

**Key Points:**

- Ionospheric feedback makes strong small-scale field-aligned currents and electric fields in fast subauroral flows with low-density troughs
- Solving the kinetic equation with these fields gives suprathermal electrons and excited neutrals explaining the subauroral arcs features
- The developed theory predicts that subauroral arcs might have the transient phase with typical aurora-like emissions fading afterward

**Correspondence to:**

E. Mishin,  
[evgeny.mishin@spaceforce.mil](mailto:evgeny.mishin@spaceforce.mil)

**Citation:**

Mishin, E., & Streltsov, A. (2022). On the kinetic theory of subauroral arcs. *Journal of Geophysical Research: Space Physics*, 127, e2022JA030667. <https://doi.org/10.1029/2022JA030667>

Received 18 MAY 2022

Accepted 1 AUG 2022

**Author Contributions:**

**Investigation:** Evgeny Mishin, Anatoly Streltsov

**Writing – original draft:** Evgeny Mishin, Anatoly Streltsov

**Writing – review & editing:** Evgeny Mishin, Anatoly Streltsov

**Abstract** We report on a novel scenario of subauroral arcs within strong subauroral ion drifts (SAID)-STEVE and Picket Fence. Their explanation requires a local source of low-energy,  $\epsilon < 18.75$  eV, suprathermal electrons, and  $N_2$  vibrational and electronic excitation below  $\sim 270$  km. We show that the ionospheric feedback instability in strong SAID flows with depleted density troughs generates intense, small-scale field-aligned currents and parallel electric fields below the  $F_2$  peak. With these fields, we employed a rigorous numerical solution of the Boltzmann kinetic equation for the distribution of ionospheric electrons and determined the power going to excitation and ionization of neutral gas (the energy balance). The obtained suprathermal electron population and energy balance at altitudes of  $\sim 130$ – $140$  km are just what is necessary for Picket Fence. Concerning STEVE, the kinetic theory predictions are in a good qualitative agreement with its basic features, such as the enhanced continuum emissions. Besides, the theory predicts that subauroral arcs might have the transient phase with typical aurora-like emissions that fade out afterward.

**Plain Language Summary** Subauroral arcs radically different from usual aurora occur inside subauroral flows (SAID) with depleted density and high electron temperature. Their interpretation requires specific local distributions of electrons and vibrationally excited neutrals. In Picket Fence at  $\sim 130$ – $140$  km, the electron distribution function (EDF) is enhanced at energies  $< 18.75$  eV. The ionospheric feedback instability within SAID generates small-scale field-aligned currents and electric fields nonlinearly increasing with the SAID and depletion magnitude. Via the EDF, these fields control the power going to the excitation of neutrals (the energy balance). Because the EDF deviates from a Maxwellian, we use a rigorous solution of the Boltzmann kinetic equation with the modeled fields. The resulting energy balance at  $\sim 130$ – $140$  km corresponds to the EDF and excited neutral species required for Picket Fence. The theory predictions qualitatively agree with the STEVE features above 200 km. Besides, inside SAID with deep depletions the EDF contains many ionizing electrons at  $\sim 170$ – $200$  km. Additional ionization changes the initial density profile and the instability development will likely be saturated when the generated fields in the whole altitude range reduce below the ionization threshold. In other words, subauroral arcs might have the transient phase with typical aurora-like emissions that fade out afterward.

### 1. Introduction

East-west-aligned, mauve “ribbons” equatorward of the auroral zone have long been known under a quaint name “Steve.” Those are related to subauroral ion drifts (SAID) with the westward speeds of  $|\mathbf{v}_w| = |\mathbf{E}_\perp \times \mathbf{b}_0| \sim 4 - 6$  km/s ( $\mathbf{b}_0 = \mathbf{B}_0/B_0$ ), elevated electron temperatures,  $T_e$ , up to  $\sim 10^4$  K, and deep density troughs,  $n_e \leq 10^4$  cm<sup>-3</sup> (e.g., Archer, Gallardo-Lacourt, et al., 2019; MacDonald et al., 2018). Due to large velocities and strongly elevated  $T_e$ , the Steve arcs were dubbed strong thermal emission velocity enhancement (STEVE). An extensive account of earlier works prior to the “STEVE era” is given in Henderson (2021) and Hunnekuhl and MacDonald (2020). STEVE is the premidnight, substorm recovery phenomenon (Gallardo-Lacourt, Nishimura, et al., 2018) lacking  $> 50$  eV electrons (Chu et al., 2019; Gallardo-Lacourt, Liang, et al., 2018; Nishimura et al., 2019). STEVE’s unusual color is determined by a 400–800 nm continuum (Gillies et al., 2019).

Sometimes, STEVE is accompanied by a greenish-rayed arc resembling a picket fence, hence termed Picket Fence. Liang et al. (2019) reported on a subauroral arc with two emission structures at altitudes  $h \leq 150$  and  $\sim 250$  km. The latter contained substantial enhancement of the redline emission from the  $O(^1D)$  state over background. Archer, St.-Maurice, et al. (2019) estimated the height extent of STEVE and Picket Fence on nearby or perhaps the same magnetic field lines as 130–270 and 97–150 km, respectively.

During a STEVE-Picket Fence event captured in the northern hemisphere (NH) on 8 May 2016, Nishimura et al. (2019) used DMSP F17, THEMIS-E (TH-E), and Swarm A in the southern hemisphere (SH) close to the NH track of Swarm-B. The Swarm satellites detected similar SAID channels, typical of the SAID events, including particle distributions near the magnetic equator (e.g., Mishin, 2013). The F17 and TH-E electric fields exhibited a double-SAID structure. The outermost SAID was magnetically conjugate to Picket Fence and nearly collocated with enhanced energetic electron precipitation (“bump”),  $\sim 10$  keV, in the plasmasphere and top ionosphere. The innermost SAID channel without energetic electrons was conjugate to STEVE. Thus, Nishimura et al. (2019) concluded that Picket Fence is, in fact, a rayed subauroral aurora.

On the other hand, auroral emissions produced by collisional degradation of energetic electrons exhibit the well-defined spectrum. It is formed mainly by the so-called degradation spectrum of suprathermal electrons (e.g., Banks et al., 1974; Konovalov & Son, 2015):

$$F_s(\epsilon) = \frac{m_e^2}{2\epsilon} \Phi_e(\epsilon) \approx \frac{3}{2\pi v_c^3} n_s \begin{cases} (\epsilon_c/\epsilon)^{4.5} & \text{at } \epsilon_c \leq \epsilon \leq \epsilon_c^* \\ (\epsilon_c/\epsilon_c^*)^{4.5} (\epsilon_c^*/\epsilon)^{3.5} & \text{at } \epsilon_c^* < \epsilon < 300 \text{ eV} \end{cases} \quad (1)$$

Here  $v_c = \sqrt{2\epsilon_c/m_e}$ ,  $\epsilon_c \approx 5$  eV,  $\epsilon_c^* \approx 20$  eV,  $n_s \approx (25-30)n_b$ ,  $n_b$  is the density of precipitating energetic electrons with the omnidirectional differential number flux  $\Phi_e(\epsilon)$ .

However, in the Picket Fence events (Mende & Turner, 2019; Mende et al., 2019) the blue-line emission at 427.8 nm from the  $N_2^+ 1N(0,1)$  level was lacking, while the first positive band ( $N_2 1P$ )  $\geq 650$ -nm emissions via  $B^3\Pi_g \rightarrow A^3\Sigma_u^+ + h\nu$  transition and the green line from O(<sup>1</sup>S) were abundant. That is, the suprathermal population significantly increased over  $F_s(\epsilon)$  (Equation 1) between  $\sim \epsilon_c$  and the  $N_2^+ 1N$  threshold,  $\epsilon_b = 18.75$  eV. Note, only  $\approx 2.3\%$  of the  $N_2$  ionization radiates the blue line. Another possible source of the green-line emission is collisional quenching of the metastable  $N_2(A^3u^+)$  state by atomic oxygen leading to energy transfer to O(<sup>1</sup>S). This reaction leads mainly to the green color below  $\sim 200$  km because the metastable O(<sup>1</sup>D) state is strongly quenched.

Mishin and Streltsov (2019; henceforth, MS19) have shown that the presence of the energetic precipitating “bump,” which enhances the Hall conductance ( $\Sigma_H$ ) over the Pedersen conductance ( $\Sigma_p$ ), leads to the Picket Fence structure. MS19 employed a three-dimensional (3D), model (Jia & Streltsov, 2014) of the ionospheric feedback instability (IFI) in the SAID channel. In a 2D system, without the Hall current, east-west-aligned “sheets” of small-scale upward and downward FACs carried by dispersive Alfvén waves are closed by the meridional Pedersen current. The characteristic scale of the resulting series of east-west-aligned strips is of the order of the most unstable wavelength. The Hall conductance ( $\Sigma_H > \Sigma_p$ ) makes a 3D system by rotating the IFI-generated ionospheric currents and electric fields, which results in a chain of small-scale vortices resembling a series of “pickets” within the SAID channel (e.g., MS19, Figure 3).

Furthermore, contrary to the thermal excitation, the O(<sup>1</sup>D) redline emission in STEVE is on average less intense than in SAR arcs with significantly smaller temperatures. MS19 (Figure 4) resolved this controversy using the kinetic solution (Mishin et al., 2000, 2004), which shows that the  $N_2$  “vibrational barrier” practically eliminates the thermal excitation in STEVE because of the electron distribution function (EDF) “bite-out.” The term “vibrational; barrier” designates a greatly enhanced cross-section of  $N_2$  vibrational excitations,  $\sigma_v(\epsilon)$ , in the energy range  $\epsilon > \epsilon_1 = \sqrt{m_e v_1^2} \approx 1.9$  eV and  $\epsilon \leq \epsilon_2 \approx 3.5$  eV. Based on this electron kinetic effect, MS19 argued that the STEVE continuum is determined by the suprathermal electron population.

Therefore, the question arises about the source of suprathermal electrons at the STEVE and Picket Fence altitudes. It is known that suprathermal electrons,  $\epsilon \sim 10-300$  eV, in the SAID channel in the top ionosphere come from the turbulent plasmasphere boundary layer (e.g., Mishin, 2013). However, this population degrades along the path to the F region, not to mention the E region (see Khazanov et al., 2017). The obvious corollary to the above is that an unknown local source of low-energy,  $\epsilon < 18.75$  eV, suprathermal electrons and  $N_2$  excitation operates in the SAID channel below  $\sim 270$  km. Mishin and Streltsov (2021, Chapter 5.3; hereafter MS21, Ch.5.3) suggested to invoke parallel electric fields,  $E_{\parallel}$ , resulting from an instability driven by intense FACs. This is most likely (Voronkov & Mishin, 1993) in a plasma density depletion (a so-called “valley”) of  $n_e^{(v)} \sim 10^3 \text{ cm}^{-3}$  between

$\geq 120$  and  $\leq 200$  km (Titheridge, 2003). In addition,  $E_{\parallel}$  is the intrinsic feature of the IFI-generated small-scale dispersive Alfvén waves.

This paper investigates the suprathermal electron population produced by small-scale parallel electric fields generated by the IFI inside a strong westward flow channel with a deep density trough. First, we numerically simulate the IFI development with the input parameters, such as the driving poleward electric field and the electron density, similar to those in the STEVE region in the top ionosphere. The density altitude profile in the STEVE region has not yet been determined, especially below the  $F_2$  peak. Thus, we assume an arbitrary profile based on the nighttime values (e.g., Titheridge, 2003) and do not attempt to address specific experimental details but rather focus on the basic features of the simulation. In any case, as noted by MS19, the equilibrium plasma and neutral density profiles in the SAID/STEVE region would be modified by the upwelling in the atmosphere due to enhanced ohmic heating.

We show that the IFI driven by strong electric fields within a low-density trough leads to greatly enhanced  $E_{\parallel}$  and the parallel voltage below the nighttime  $F_2$  peak. The presence of the valley further increases  $E_{\parallel}$  and the voltage. The obtained electric fields are used as the input into the Boltzmann kinetic equation to find the EDF and the power going to excitation and ionization of neutral species. The simulation results show the feasibility of this mechanism for subauroral arcs. In particular, it creates the population of suprathermal electrons and  $N_2$  excitation in good quantitative agreement with that required for Picket Fence. As far as the STEVE spectrum is concerned, the kinetic theory predictions are in a qualitative agreement with its basic features.

## 2. Ionospheric Feedback Instability in Strong SAID

We calculate the parallel electric field created by the IFI in a fast SAID channel with a deep density trough. The ionospheric feedback process amplifies small-scale Alfvén waves by virtue of over reflection from the ionosphere, which is caused by the shear convection flow due to the altitudinal dependence of ion-neutral collisions. In particular, for E-region plasma densities,  $n_{0E} \leq 10^4 \text{ cm}^{-3}$ , the IFI threshold for 1–10 km wavelengths is approximately  $E_{th} \approx 50\Omega_{ci}/\nu_{i0}$  mV/m (Trakhtengerts & Feldstein, 1991). Here,  $\nu_{i0}$  ( $\Omega_{ci}$ ) is the ion-neutral collision (ion cyclotron) frequency at 105–110 km. In a 2D model, without the Hall current, the Pedersen (meridional) current,  $\mathbf{J}_p = \Sigma_p \mathbf{E}_{\perp}$ , has the form of a strip between the east-west aligned sheets of upward and downward FACs enclosing the flow channel. The IFI “splits” the initial strip into a series of small-scale strips determined by the most unstable wavelength. The resulting fine meridional structure of the FACs inside the STEVE channel is consistent with the Swarm-A FACs in the Nishimura et al., 2019 (Figure 2j) event.

A two-fluid MHD model (e.g., Streltsov & Mishin, 2018; hereafter SM18; Streltsov et al., 2012) consists of the “magnetospheric” and “ionospheric” parts. The former describes dispersive Alfvén waves in an axisymmetric dipole magnetic field using equations for the electron parallel momentum and continuity of the plasma density,  $n$ , and FACs,  $j_{\parallel} = -n_e u$ . Here  $u$  is the parallel component of the electron velocity.

We take a meridional (poleward) trapezoidal electric field,  $E_x(x)$ , centered at  $L = 4.9$  and consider a 2D problem justified for azimuthally extended STEVE arcs. As in SM18, the computational domain represents a 2D slice of the axisymmetric dipole magnetic field between magnetic shells 4.7 and 5.1. The ionospheric boundaries of the domain are set at 110-km altitude. The vertical size of the conducting portion of the E-region ionosphere is much less than the parallel wavelength, so it is taken as a narrow layer with the uniform density and electric field. In this case, the simplest (so-called electrostatic) boundary conditions are derived by integrating the current continuity equation,  $\nabla \cdot \mathbf{j} = 0$ , over the conducting (dynamo) layer with the effective thickness of  $h \approx 10\text{--}20$  km

$$\nabla \cdot (\Sigma_p \mathbf{E}_{\perp}) = \pm j_{\parallel,i} \quad (2)$$

Here  $j_{\parallel,i}$  is the FAC density on the top of the E region and the sign “+/-” in the right-hand side of Equation 2 is for the southern/northern hemisphere. The variation of the E-region density is derived by integrating the density continuity equation over the conducting layer

$$\frac{\partial n}{\partial t} + \nabla_{\perp} \cdot (n \mathbf{v}_E) = \frac{j_{\parallel}}{eh} + \alpha (n_0^2 - n^2) \quad (3)$$

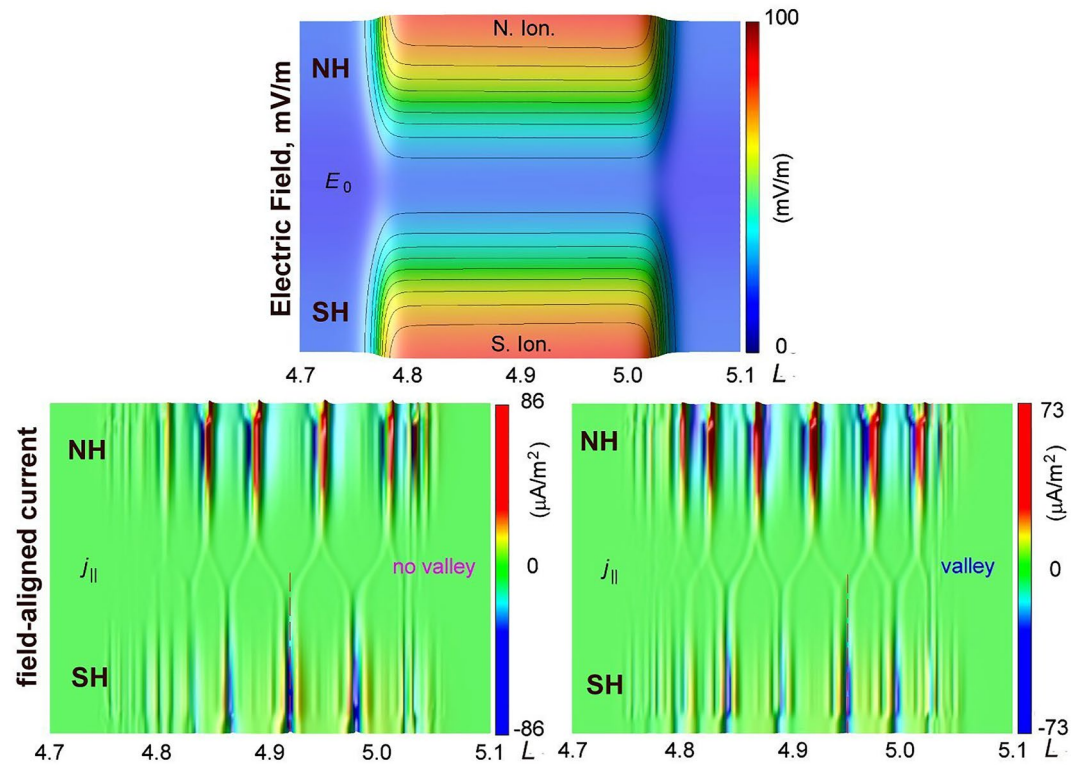


**Figure 1.** Ionospheric feedback instability simulation for  $E_0 = 100$  mV/m: The spatial distribution in the computational domain of (top) the driving electric field and field-aligned currents (left) without and (right) with the southern hemisphere valley I (see text).

Here  $v_E$  is the electric drift velocity;  $\alpha$  is the recombination coefficient; the term  $an^2$  represents losses due to the recombination, and  $an_0^2$  represents all unspecified sources of the ionospheric plasma that provide the equilibrium state of the ionosphere  $n_0$ . This system of equations forms a positive feedback loop:  $\delta\Sigma_p(\delta n_e) \rightarrow \delta j_{\parallel} \rightarrow \delta n_e$  (see, e.g., SM18 for details).

The numerical procedure used to solve the model equations has been described in detail in several papers (e.g., Streltsov et al., 2012; SM18; and references therein). Here, we present only the simulation results. As in the case considered in SM18, we assume asymmetric plasma profiles in the hemispheres. The northern hemisphere has no valley and the plasma density between 110 km (E region) and 300 km ( $F_2$  peak) increases from  $n_E^{(N)} = 10^4$  to  $n_F = 9 \times 10^4$  cm $^{-3}$ . In the runs when the southern hemisphere has no valley, the density at 110 km is taken  $n_E^{(S)} = 3 \times 10^3$  cm $^{-3}$ . In the runs with the SH valley I, we assume that  $n_e^{(v)} = \text{const} = n_E^{(S)}$  between 110 and 200 km and increases to  $n_F$  between 200 and 300 km. In the case of the SH valley II, the E-region density at  $\leq 110$  km remains  $n_E^{(S)}$  but between  $\approx 110$  and 200 km  $n_e = n_E^{(S)}/2$ ; increasing to  $n_F$  thereafter. The background plasma temperature is taken 1000 K.

Figure 1 illustrates the simulation results for  $\max(E_x(x)) \equiv E_0 = 100$  mV/m or  $\max(|v_w|) \approx 3.3$  km/s with the 2D spatial distribution in the computational domain shown in top frame. As typical (e.g., SM18), the IFI creates in both hemispheres a system of intense small-scale FACs, with downward currents ( $j_{\downarrow}$ ) dominating their upward ( $j_{\uparrow}$ ) counterparts. The current intensities of the order of 50–80  $\mu\text{A}/\text{m}^2$  are comparable to those observed in the auroral ionosphere (e.g., Akbari et al., 2022).

It is not surprising that such intense currents are associated with enhanced parallel fields, creating a 0.5–1 kV voltage,  $|\phi_{\parallel}|$ , between 110 and 200 km, as shown in Figure 2. The resulting power consumption due to Joule heating (insets) amounts to  $Q_J = j_{\parallel}E_{\parallel} = 100$ –900 nW/m $^3$ . The field magnitude,  $|E_{\parallel}|$ , and the voltage increase nonlinearly with the driving field,  $E_0$ ; that is,  $|E_{\parallel}| \propto E_0^a$  with  $a \approx 1.5$  (without) and  $\approx 1.9$  (with) the valley. Overall, in the lower-density southern hemisphere the field magnitude,  $|E_{\parallel}^{(SH)}|$ , and voltage,  $|\phi_{\parallel}^{(SH)}|$ , are larger than their northern counterparts. On the contrary, the FAC intensities,  $|j_{\parallel}^{(SH)}|$ , are smaller than  $|j_{\parallel}^{(NH)}|$ . For example, for

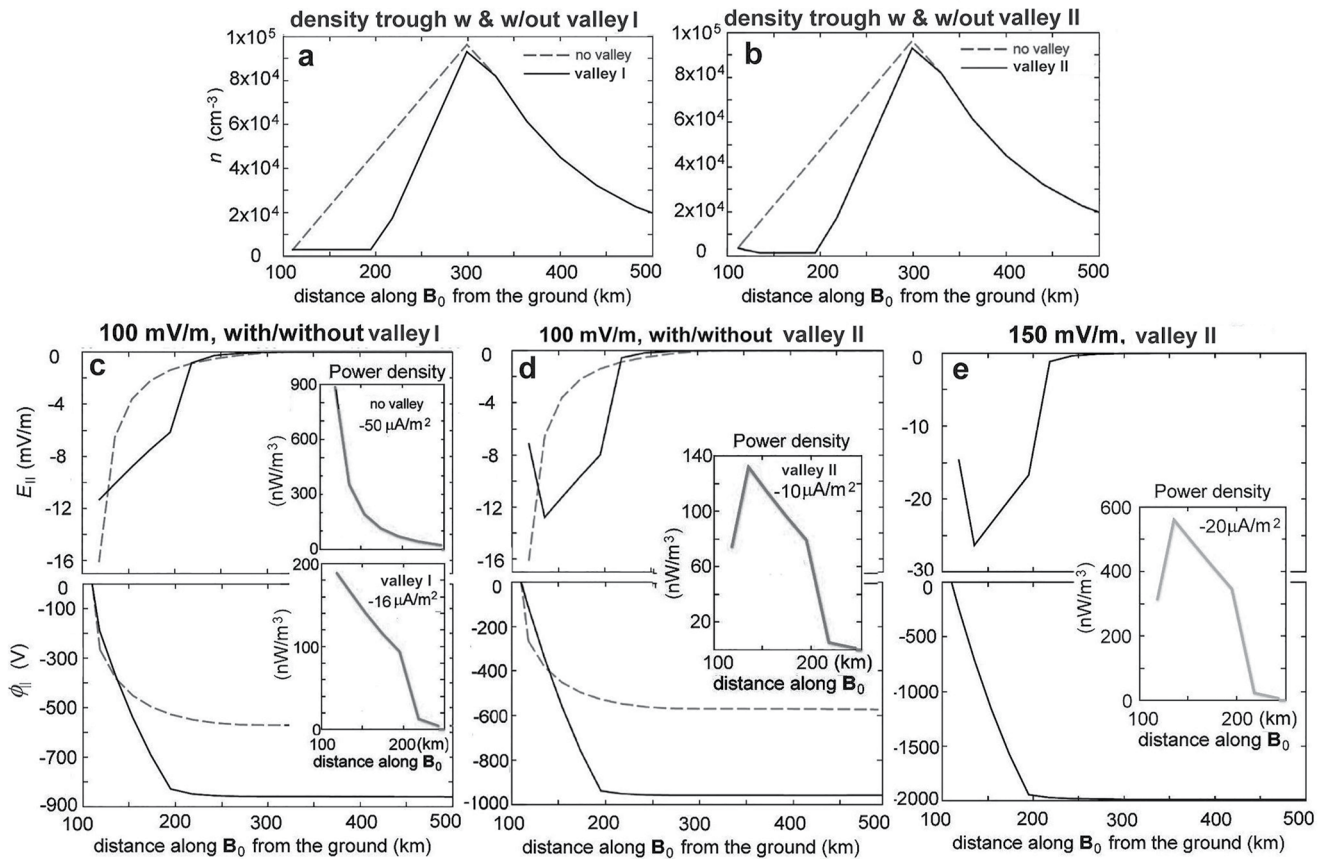


**Figure 2.** (Top) Variation along the magnetic field line of the plasma density in the trough without (the dashed line) and with (solid) the valley (a) I or (b) II; (mid)  $E_{\parallel}$  and (bottom)  $\Phi_{\parallel}$  taken in the region of the most intense southern hemisphere downward current without (dashed lines) and with (solid) the valley I and II for  $E_0 = 100$  and 150 mV/m. Insets: Variation of the corresponding power density,  $Q_j = j_{\parallel} E_{\parallel}$  in nW/m<sup>3</sup>; the FAC density averaged over the distance along  $B_0$  between 100 and 200 km,  $\langle j_{\parallel} \rangle$ , is indicated.

$E_0 = 100$  mV/m without (with) the valley we have  $E_{\parallel}^{(SH)}/E_{\parallel}^{(NH)} \approx 2$  ( $\approx 1.5$ ) and  $j_{\parallel}^{(SH)}/j_{\parallel}^{(NH)} \approx 0.7$  ( $\approx 0.23$ ). Taking the symmetric hemispheres without the valley results in about the same amplitudes as in Figure 2c without the valley but quite low electric fields and currents in the runs with the valley I and II.

It is worth to note that the amplitude of the IFI-generated small-scale FACs in the Picket Fence, 3D geometry with the Hall current is little more than in the 2D case (Jia & Streltsov, 2014; MS19). Thus, it is anticipated that simulations in a full 3D geometry for the same input conditions would give a little larger  $E_{\parallel}$  than shown in Figure 2. Given that 3D simulations are much more time consuming but the resulting fields do not qualitatively differ from the 2D case, hereinafter we use the values of  $E_{\parallel}$  from Figure 2.

Two remarks are in order before describing the effect of enhanced parallel electric fields on the ionospheric electrons and excitation of neutral gas. First, with the obtained small-scale FAC intensities, the electron parallel drift velocity,  $u = |j_{\parallel}|/n_e$ , in the depleted plasma is a fraction of the electron thermal velocity and exceeds the ion sound speed, so the ion sound instability does develop (e.g., Mikhailovskii, 1974). However, the electron gyrofrequency,  $f_{ce} \sim 1.4$  MHz, exceeds the local plasma frequency in the trough,  $f_{pe} \sim 0.3$  MHz. In this case, the excited wave spectrum is one-dimensional so that, contrary to the dense plasma with  $f_{ce} < f_{pe}$ , the anomalous resistivity is insignificant (e.g., Galeev & Sagdeev, 1984).

Second, simulations exemplified in Figure 2 also reveal the effect of the valley on the structure of ULF waves and FACs generated by the ionospheric feedback mechanism. Namely, the valley decreases the effective conductivity of the ionosphere. Its existence only in one hemisphere makes asymmetrical ionospheric boundary conditions in the global magnetospheric resonator. This asymmetry enhances the natural tendency of the ionospheric feedback mechanism to generate non-symmetrical ULF waves and field-aligned currents (Streltsov, 2018). Specifically,

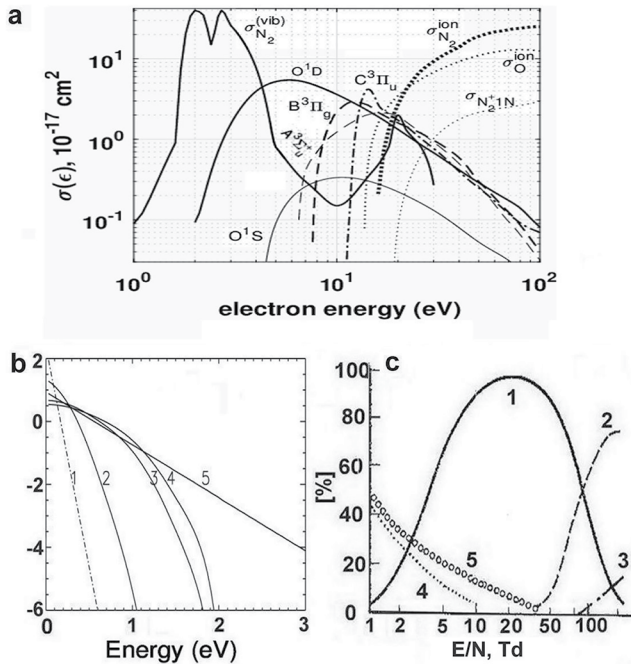


**Figure 3.** (a) Some of the basic ionization and excitation cross sections of  $N_2$  and O calculated with the Majeed and Strickland (1997) and Itikawa (2006) data. (b) Electron distribution function versus energy at  $N_{N_2}$ :  $N_{O_2}:N_O = 75:10:15$  ( $h \approx 110$  km): 1- and 5-Maxwellian at  $T_e = 360$  and 3000 K; 2-  $E_{||} = 1.1$  mV/m ( $T_e = 1290$  K); 3-  $E_{||} = 2.1$  mV/m ( $T_e = 2970$  K); 4-  $E_{||} = 4.3$  mV/m ( $T_e = 3530$  K). Adapted from Milikh and Dimant (2003). (c) Energy distribution over various channels versus  $E_{||}/N_n$  at  $N_{N_2}:N_{O_2}:N_O = 77:8:15$  ( $h \approx 120$  km): 1—vibrational levels of  $N_2$ , 2—electronic levels of  $N_2$ , 3—ionization of  $N_2$ , 4—vibrational levels of  $O_2$ , 5—gas heating. From Dyatko et al. (1989). It is assumed that the initial vibrational and fine structure populations have the gas temperature,  $T = 550$  K, while the initial electronic levels are void.

simulations show that in a strongly nonlinear stage the IFI generates so-called ULF quarter-waves first suggested by Allan and Knox (1979) and then confirmed by observations (Allan, 1983; Budnik et al., 1998; Obana et al., 2008, 2015). This problem is discussed in detail in the forthcoming paper (A. Streltsov and E. Mishin “Ionospheric feedback and the ‘quarter-period’ ULF waves”) submitted elsewhere.

### 3. Electron Distribution and the Energy Balance

The power distribution over inelastic processes (the energy balance) is calculated via the electron distribution function (EDF),  $F_e(\epsilon)$ , as follows

$$P_j = \epsilon_j \int_{\epsilon_j}^{\infty} \nu_j(\epsilon) F_e(\epsilon) d^3v = 4\pi \epsilon_j N_j \int_{\epsilon_j}^{\infty} \sigma_j(\epsilon) \Phi_e(\epsilon) d\epsilon \quad (4)$$

Here  $\nu_j(\epsilon) = v \sigma_j(\epsilon) N_j$  is the collision frequency of an inelastic process with the cross-section  $\sigma_j$  and the excitation energy  $\epsilon_j$ , as exemplified in Figure 3a. The EDF under action of the imposed electric field is a solution of the Boltzmann kinetic equation that includes elastic and inelastic processes (e.g., Capitelli et al., 2000). Figure 3b shows a rigorous numerical solution (Milikh & Dimant, 2003), which exemplifies the EDF bite-out in the E region. Figure 3c shows the energy balance explicitly calculated by Dyatko et al. (1989) with the composition typical of 110–120 km (e.g., Picone et al., 2002) for the input values of  $E_{||}/N_n \equiv \tilde{E}$  in the Townsend units: 1 [Td] =  $10^{-17}$  [V·cm<sup>2</sup>]. Here, the neutral density,  $N_n$ , is the sum of the densities of  $N_2$  ( $N_{N_2}$ ), O ( $N_O$ ), and  $O_2$  ( $N_{O_2}$ ). For reference, for  $N_n = 10^{12}$  cm<sup>-3</sup> at  $\sim 120$  km,  $\tilde{E} = 1$  Td yields  $E_{||} = 10^{-17} N_n$  [V/cm] = 1 [mV/m].

The power lost in vibrationally excited  $N_2$  ( $P_V$ ) exceeds 50% at  $\tilde{E} > \tilde{E}_V \approx 5$  Td and reaches a broad maximum  $\sim 90\%$  at  $\tilde{E}_V^{(max)} \sim 20$  Td. Excitation of the  $N_2$  electronic levels at  $\tilde{E} = \tilde{E}_A \approx 40$  and  $\tilde{E}_\Sigma \approx 100$  Td takes away the power,  $P_A \approx 3\%$  (mainly the  $A^3\Sigma_u^+$  state) and  $P_\Sigma \approx 50\%$ , respectively. Of  $P_\Sigma \approx 50\%$ , about 30% goes into the triplet  $A^3\Sigma_u^+$  (“A”),  $B^3\Pi_g$  (“B”), and  $C^3\Pi_u$  (“C”), with the excitation energies  $\epsilon_A = 6.17$  eV,  $\epsilon_B = 7.35$  eV, and  $\epsilon_C = 11.03$  eV, respectively. At the same time, about 10% goes to the electronic levels of  $O_2$  and O (not shown), mainly  $O(^1D)$  with  $\epsilon_r = 1.96$  eV and  $O(^1S)$  with  $\epsilon_g = 4.17$  eV. Note that the ionization of  $N_2$  (curve 3) begins at  $\tilde{E} > 90$  Td and amounts to  $P_{ion} \sim 2\%$  at 100 Td. That is, the ionizing population,  $\epsilon > \epsilon_{ion} = 15.6$  eV, appears at  $\tilde{E} > \tilde{E}_{ion} \approx 90$  Td.

Note, the suprathermal tail at  $\tilde{E}_A \leq \tilde{E} \leq \tilde{E}_{ion}$  is confined within the energy range optimal for Picket Fence,  $\epsilon_2 < \epsilon \leq \epsilon_{ion}$ , and a significant power is spent on the  $N_2$  excitation, as well. At  $h \sim 120$  km, the above values of  $\tilde{E}_V$ ,  $\tilde{E}_A$ , and  $\tilde{E}_{ion}$  correspond to the magnitudes,  $E_V = 5$ ,  $E_A = 40$ , and  $E_{ion} = 90$  mV/m, respectively, and thus the IFI generated fields in Figure 2 at  $E_0 \leq 150$  mV/m excite mainly  $N_2$  vibrational states. If the energy balance at higher altitudes remains the same as at 120 km, then the corresponding values will reduce as  $N_n(h)/10^{12}$ . Particularly, for  $N_n = 10^{11}$  ( $10^{10}$ ) cm<sup>-3</sup>, that is,  $h \approx 130$ –135 (170–175) km, we get  $E_V = 0.5$  (0.05),  $E_A = 4$  (0.4), and  $E_{ion} = 9$  (0.9) mV/m. Therefore, as one can see from Figure 2, the generated fields in the trough exceed  $E_{ion}$  at and above 130 km with the valley and at  $\geq 170$  km without the valley.

Most notably, for  $E_0 = 100$  mV/m in the density trough without the valley, we get at  $h \sim 130$  km  $E_A < E_{||} \approx \frac{1}{2} E_{ion}$ , with  $P_V \leq 80\%$  and  $P_\Sigma \geq 10\%$ . Further, the neutral density usually obeys the barometric law and hence decreases with altitude faster than  $|E_{||}|$  in Figure 2. Accordingly, the Picket Fence-required conditions, that is, the enhanced population between  $\sim \epsilon_c$  and  $\epsilon_b$  and the excited  $N_2$  triplet, will be formed at altitudes  $130 \leq h_{pf} \leq 140$  km. Here, collisional quenching of the metastable  $O(^1D)$  state severely suppresses the redline emission (e.g., Mishin et al., 2004, Figure 5). Therefore, the green-line and  $N_2$  1P emissions will make the Picket Fence-like color in accordance with the observations (Mende & Turner, 2019; Mende et al., 2019). Yet, we have to ensure that the

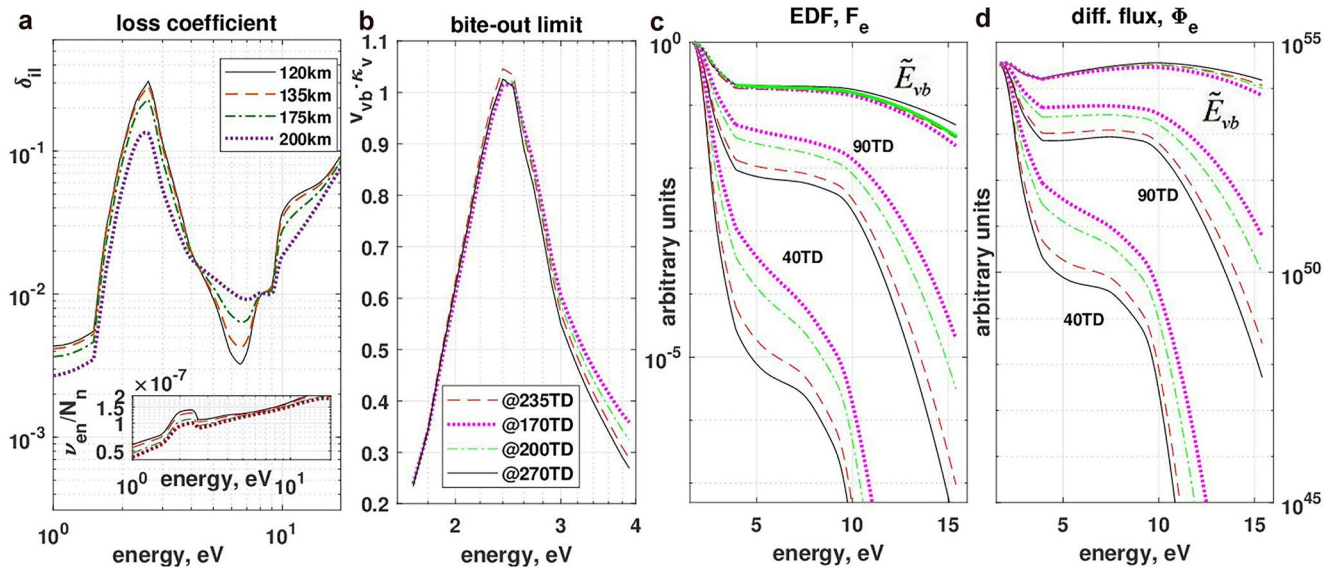


**Figure 4.** The energy dependence at various altitudes of (a) the inelastic loss coefficient,  $\delta_{||}(\epsilon) = \nu_{ij}(\epsilon)/\nu_{en}(\epsilon)$  calculated with the Majeed and Strickland (1997) and Itikawa (2006) data; (b) the product  $\nu_{vb}k_v(\epsilon, h, \tilde{E}_{vb}(h))$  at the vibrational barrier (see text); (c) the electron distribution function,  $F_e(\epsilon)$ , and (d) the omnidirectional differential number flux,  $\Phi_e(\epsilon)$ , for  $\tilde{E}_A$ ,  $\tilde{E}_{ion}$ , and  $\tilde{E}_{vb}(h)$ . Inset: The transport collision frequency,  $\nu_{en}(\epsilon)/N_n$ , per one molecule. The altitudes are indicated by the line style and color, and the electric field magnitudes are shown in Td units.

EDF and the corresponding energy balance at these altitudes remain close to those at 120 km. This assertion is addressed next.

Strictly speaking, the EDF and the energy balance at any given altitude should be calculated with the pertinent neutral composition. Such a formidable task is beyond the scope of this paper aimed at the basic qualitative outcomes of the IFI-generated electric fields in a given density profile. Nonetheless, we can make ballpark estimates with the aid of an analytic solution of the Boltzmann kinetic equation. In the  $N_2$  vibrational barrier,  $\epsilon_1 \leq \epsilon \leq \epsilon_2$ , we have  $\epsilon\sigma_v(\epsilon)F_i(\epsilon) \gg (\epsilon + \epsilon_v)\sigma_v(\epsilon + \epsilon_v)F_i(\epsilon + \epsilon_v)$ , where the energy quantum  $\epsilon_v \approx 0.29(V + 1/2)$  eV. This inequality allows using the discrete losses approximation for the collision integral,  $St_{dl}(F_e) \approx -\nu_{il}(\epsilon)F_e \approx -\nu\sigma_v(\epsilon)N_{N_2}F_e$ , yielding (cf. Gurevich, 1978, Equation 2.154)

$$\frac{\partial}{\partial t} F_i(v) - \frac{\partial}{v^2 \partial v} v^2 D_{||} \frac{\partial}{\partial v} F_i(v) = St_{dl}(F_e) \approx -\nu_{il}(\epsilon)F_i(v) \quad (5)$$

Here  $D_{||} = \frac{1}{3}\nu_e(\epsilon)u_{||}^2(\epsilon)$  and

$$u_{||}(\epsilon) = eE_{||}/m_e\nu_{en}(\epsilon) \approx 2.7 \times 10^6 \epsilon^{-1/2} \tilde{E} / (\rho_1\tilde{\sigma}_1 + \rho_2\tilde{\sigma}_2) \text{ [cm/s]} \quad (6)$$

Here  $\rho_{1(2)} \approx N_{1(2)}/(N_1 + N_2)$  is the abundance of molecular nitrogen (“1”) and atomic oxygen (“2”) and the corresponding transport cross-sections  $\sigma_j = 10^{-16}\tilde{\sigma}_j \text{ cm}^2$ ; the energy  $\epsilon$  is in eV. The contribution of molecular oxygen—a minor species at  $h > 120$  km—is neglected, as well as Coulomb collisions. As  $\max(\sigma_v) = \sigma_v^{(vb)} \approx 4 \times 10^{-16} \text{ cm}^2$  exceeds the  $O(^1D)$  excitation cross-section,  $\sigma_D(3eV) \equiv \sigma_D^{(vb)}$  by a factor of  $\sim 30$  (Figure 3a), the vibrational barrier remains the key feature that shapes the EDF at altitudes with  $\rho_2/\rho_1 < 30$ , that is, below  $\sim 300$  km (e.g., Mishin et al., 2000).

Disregarding inelastic collisions yields a stationary solution of Equation 5 with the constant flux of heated electrons into the suprathermal tail

$$J_t = v^2 D_{||} \frac{\partial}{\partial v} F_i(v) = \text{const}(v) \quad (7)$$

Inelastic losses prevent the tail stretching toward large energies, viz., “bite out” the tail population. This process is usually described considering the kinetic equation as the stationary Schrödinger equation in

the velocity space, where inelastic collisions represent a potential barrier. The effective “potential” is  $\kappa_v^2 \equiv v_{il}/D_{\parallel} = 3v_{il}(\epsilon)/v_e(\epsilon)u_{\parallel}^2(\epsilon) = 3\delta_{il}/u_{\parallel}^2(\epsilon)$ , where  $\delta_{il}(\epsilon)$  is the coefficient of inelastic losses. The tail expansion slows down when  $\kappa_v^2(\epsilon_1) \gg (2\epsilon_V/m_e)^{-1} \equiv v_{vb}^{-2}$  or

$$\delta_{il}^{(vb)} \equiv v_{il}(\epsilon_1)/v_e(\epsilon_1) \gg \frac{1}{6}m_e u_{\parallel}^2(\epsilon_1)/\epsilon_V \quad (8)$$

Owing to this condition, Equation 5 can be solved in the quasi-classical approximation (cf. Gurevich, 1978, Equation 2.166)

$$F_i(\epsilon) \approx \frac{C_t}{v(\kappa_v D_{\parallel})^{1/2}} \exp\left(-\int_{v_1}^v \kappa_v(v)dv\right) \quad (9)$$

The constant  $C_t$  is defined by the matching condition,  $F_i(v_1) = F_0(v_1)$ , with the EDF of the bulk electrons at  $\epsilon < \epsilon_1$ . Outside the barrier, at  $\epsilon < \epsilon_1$  and  $\epsilon > \epsilon_2$  (but  $< \epsilon_{ion}$ ), the lost energy quanta are small,  $\Delta\epsilon_j \ll \epsilon$ , so the continuous loss approximation is applicable:

$$St_{cl}(F_e) \approx \frac{1}{2v^2} \frac{\partial}{\partial v} (v^3 L_{il}(v)F_e)$$

Here  $L_{il}(v) = \sum_j \nu_j(v)\epsilon_j/\epsilon = \delta_{il}(\epsilon)\nu_{en}(\epsilon)$  is the loss function and  $\nu_j$  is the excitation rate, which is determined at  $\epsilon_{ion} > \epsilon > \epsilon_2$  mainly by excitation of the  $N_2$  triplet, as well as  $O(^1D)$  and  $O(^1S)$  (Figure 4a). Substituting  $St_{cl}(F_e)$  for  $ST_{dl}(F_i)$  in Equation 5 yields a steady state solution

$$F_e(\epsilon) = F_i(\epsilon_2) \exp\left(-\frac{3}{2} \int_{\epsilon_2}^{\epsilon} d\epsilon \delta_{il}(\epsilon)/m_e u_{\parallel}^2\right) \quad (10)$$

Figure 4 presents the dependence of the key variables on the electric field at various altitudes. The reduced transport frequency in the vibrational barrier decreases with altitude as  $\rho_1(h) (1 + \gamma_2 \rho_2(h)/\rho_1(h))$ , where  $\gamma_2 = \sigma_2/\sigma_1 \approx 1/3$  at  $\epsilon \sim 2-3$  eV. The contribution of  $\rho_2(h) (\sigma_D + \sigma_S)$  increases with altitude, while the triplet contribution,  $\sim \rho_1(h)\sigma_{\Sigma_2}$ , decreases. This makes the depth of the local minimum of  $\delta_{il}(h)$  at 6–7 eV decrease with  $h$  and, similarly, the rise at  $>10$  eV slow down. Figure 4b shows the variation of  $v_{vb}\kappa_v(\epsilon, \tilde{E})$  with  $\tilde{E} = \tilde{E}_{vb} \approx 350\rho_1 \sqrt{1 + \gamma_2 \rho_2/\rho_1}$  Td—the upper limit for the “bite-out” approximation. Here,  $\tilde{E}_{vb}(h)$  is determined from the violation of Equation 8, as illustrated the evolution of the EDF,  $F_e(\epsilon)$ , and number flux,  $\Phi_e(\epsilon) = 2\epsilon F_e(\epsilon)/m_e^2$ , at  $\tilde{E} = \tilde{E}_A, \tilde{E}_{ion}$ , and  $\tilde{E}_{vb}(h)$  (cf. Gurevich, 1978, Figure 8).

The most important conclusion for the Picket Fence mechanism is that for a broad range of the electric field magnitudes the curves for 120 and 135 km in Figure 4c are close. Accordingly, we can deduce that the energy balance at 135 km remains nearly the same as at 120 km, which was to be demonstrated to explain the Picket Fence color near  $h_{pf}$ . Notwithstanding that the perturbed atmosphere's upwelling might change the conditions, the estimated altitude range is also consistent with the observations (e.g., Archer, St.-Maurice, et al., 2019; Liang et al., 2019).

Further, in photochemical equilibrium, the volume emission rate (VER),  $\eta_{\lambda}$ , is calculated from

$$\eta_{\lambda} = A_{\lambda} \cdot [X_{\lambda}] = A_{\lambda} \frac{q_{\lambda}}{L_{\lambda} + A_{\Sigma\lambda}} [\text{cm}^{-3}\text{s}^{-1}] \quad (11)$$

Here  $[X_{\lambda}]$  stands for the density of the excited species in  $\text{cm}^{-3}$ ;  $A_{\lambda}$ ,  $q_{\lambda}$ , and  $L_{\lambda}$  are the Einstein transition probabilities (in  $\text{s}^{-1}$ ), excitation, and loss rates, respectively. For the  $B^3\Pi_g$  state, we have  $A_{\Sigma B} = A_B \gg L_B$  yielding  $\eta_B \approx q_B$ . For  $O(^1S)$  green line (“g”) with  $A_{\Sigma g} \approx 1.1A_g \gg L_g$  at  $h \geq h_{pf}$ , we obtain  $\eta_g \approx 0.9q_g$ . For the metastable  $O(^1D)$  state (“r”) with  $A_r \approx \frac{7}{9}A_{\Sigma r} \approx 0.007 \text{ s}^{-1}$  and the collisional quenching rate  $L_r(h_{pf}) \geq 1 \text{ s}^{-1}$  (e.g., Mishin et al., 2004, Figure 5), we get  $\eta_r \leq 0.007q_r$ . At  $\tilde{E} \rightarrow \tilde{E}_{ion}$ , the flux  $\Phi_e(\epsilon)$  tends to a quasi-plateau between  $\epsilon_2 < \epsilon \leq \epsilon_C$  (Figure 4c). The abrupt decrease thereafter is mainly due to the excitation of the  $C^3\Pi_u$  state.

Thus, the excitation rates,  $q_{\lambda} \sim N_n \rho_2 \int \Phi_e(\epsilon, h) \sigma_{\lambda}(\epsilon) d\epsilon$ , are determined by the area integral  $\int \sigma_{\lambda}(\epsilon) d\epsilon$  over the “plateau.” Calculating that one with the cross-sections in Figure 3a gives  $q_r \approx 20q_g$  and  $q_A \approx q_B \approx 2(\rho_1/\rho_2)q_g$ ,

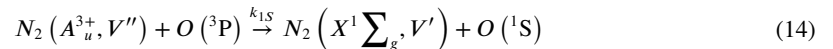
such that  $\eta_r \leq 0.16\eta_g$  and  $\eta_B \approx 2(\rho_1/\rho_2)\eta_g$ . Integrating  $\eta_\lambda(h)$  Equation 11 along the line of sight gives the surface brightness

$$I_\lambda = 10^{-6} \int_{h_{\min}}^{h_{\max}} \eta_\lambda(h) dh \text{ [R]} \quad (12)$$

(1 Rayleigh =  $10^6$  photon/cm<sup>2</sup>s). It can be estimated using the power density obtained in Figure 2c, as follows. The average total power consumed near  $h_{\text{pf}}$  is of the order of  $Q_J \sim 0.3 \mu\text{W/m}^3$ . A fraction of that,  $Q_{\text{tot}} \sim 0.2Q_J$ , splits between the N<sub>2</sub> triplet and O(<sup>1</sup>D) and O(<sup>1</sup>S) states, with each state taking the share  $Q_j \approx \epsilon_j q_j$ . Using the obtained relation between the excitation rates yields

$$Q_{\text{tot}} \approx \epsilon_r (q_r + q_g \epsilon_g / \epsilon_r + q_A \epsilon_A / \epsilon_r + q_B \epsilon_B / \epsilon_r) \approx q_g \epsilon_r [22 + 13 (\rho_1 / \rho_2)] \quad (13)$$

With  $\rho_1(h_{\text{pf}}) \sim 2\rho_2(h_{\text{pf}}) \sim 2/3$ , Equation 13 yields the excitation rates  $q_g \sim 4 \times 10^3 \text{ cm}^{-3}\text{s}^{-1}$  and  $q_A \approx q_B \approx 4q_g$ . Then, for the emitting layer of  $\Delta h \sim 5$ -km thick, we get the brightness of the green-line and N<sub>2</sub>1P band emissions of  $I_g^{(e)} \sim q_g \Delta h \sim 2 \text{ kR}$  and  $I_{1P}^{(e)} \sim 4I_g^{(e)} \sim 8 \text{ kR}$ , respectively. However, in addition to electron impact, O(<sup>1</sup>S) appears via collisional quenching of the N<sub>2</sub> ( $A_u^{3+}$ ) state by atomic oxygen



The rate coefficient at  $V''=0$  is  $k_{1S} \approx 2 \cdot 10^{-11} \text{ cm}^3/\text{s}$  (Piper, 1992). In addition to the direct excitation at  $q_A \approx 4q_g$ , the N<sub>2</sub>1P source,  $B^3\Pi_g \rightarrow A^3\Sigma_u^+ + h\nu$ , adds the rate  $q_B \approx q_A$ . Given that the metastable  $A^3\Sigma_u^+$  state has  $A_{\Sigma^+} = A_A \approx 0.4 \text{ s}^{-1}$  and  $L_A \approx 8 \times 10^{-11} \rho_2 N_n \approx 1.5 \text{ s}^{-1}$  at  $h_{\text{pf}}$ , Equations 11 and 14 yield the O(<sup>1</sup>S) excitation rate twice as much as the electron impact rate,  $q_g$ . Thus, the total green-line brightness amounts to  $I_g^{(\text{tot})} \sim 3I_g^{(e)} \sim 6 \text{ kR} \sim 0.75 I_{1P}^{(e)}$ . That is, in agreement with the Mende et al. (2019) and Mende and Turner (2019) conclusion, the green-line and N<sub>2</sub>1P band emissions dominate the Picket Fence spectrum near  $h_{\text{pf}}$ ; the Vegard-Kaplan band via  $A^3\Sigma_u^+ \rightarrow X^1\Sigma_g^+$  transition are also present. For comparison, Nishimura et al. (2019) estimated the green-line emission produced by collisional degradation of precipitating electrons in the 8 May 2016 Picket Fence event as  $I_g^{(\text{aur})} \sim 2.5 \text{ kR}$ .

However, such a quantitative comparison with the energy balance in Figure 2c is less reliable for STEVE in the F<sub>2</sub> region. Here, an accurate account of the effect of electron-electron collisions on the EDF should be taken, such as in, for example, Mishin et al. (2000) approximate solution after swapping  $e^2 E_{\parallel}^2 / m_e v_e^2$  for  $W/n_0$ . Even so, we anticipate this effect in a low-density trough to become significant only near  $\sim 300$  km and above. We plan to explore that in the future. At present, we can draw some qualitative conclusions based on nearly the same shape of  $F_e(\epsilon, h)$  and  $\Phi_e(\epsilon, h)$  in Figure 4 at higher and lower altitudes, as follows. At  $\tilde{E} < \tilde{E}_{\text{vb}}(h)$ , the N<sub>2</sub> excitation remains dominant but the electron population permeating the barrier and forming a quasi-plateau increases with altitude. This makes the portion going to the excitation of the N<sub>2</sub> triplet and oxygen states increase. The latter, as follows from Equation 13, dominates at altitudes where  $\rho_1 < 1.7\rho_2$ , viz., above  $\sim 200$  km. Here, the O(<sup>1</sup>D) quenching rate reduces (e.g., Mishin et al., 2004, Figure 5) so that the redline emission dominates the green line, that is,  $\eta_r > \eta_g$ . At the same time, as discussed by MS19, transitions between vibrationally excited triplet states facilitate the STEVE continuum, which makes its mauve color (Gillies et al., 2019).

The decrease of the IFI generated field above  $\sim 250$  km (Figure 2) places the upper limit of the altitude range for STEVE. Similar to Picket Fence, though with the possible atmosphere's upwelling, these predictions are consistent with the observations (e.g., Archer, St.-Maurice, et al., 2019; Liang et al., 2019).

A final remark is in order. A valley is a common feature of the premidnight subauroral ionosphere (e.g., Titheridge, 2003), which is further deepened inside the SAID channel. As one can see from Figure 2, the generated fields in the trough exceed  $E_{\text{ion}}$  at and above 130 km with the valley and at  $\geq 170$  km without the valley. Therefore, we expect that ionization by the suprathermal electrons will swiftly increase the plasma density at these altitudes. That is, a strongly depleted density profile is not sustainable inside strong flow channels. It is reasonable to assume that the IFI development in the evolving density profile will be saturated when the generated fields in the whole altitude range reduce to  $|E_{\parallel}| \leq E_{\text{ion}}$ . Therefore, we suggest that the subauroral arc has the transient phase. Namely, the initial "adjustment" of the density profile features also the N<sub>2</sub><sup>+</sup>1N blue- and violet-line emissions of the intensity fading out with time. In other words, the initial subauroral emission spectrum consisting of all

typical auroral lines gradually reduces to the subauroral arc spectrum discussed above. Such a transition can be revealed in dedicated high-temporal resolution observations.

#### 4. Conclusions

The focus of this paper is the suprathermal electron population inside SAID channels with deep density troughs. This is typical for the STEVE and Picket Fence arcs whose interpretation requires a local source of low-energy,  $\leq 15.6$  eV, suprathermal electrons, and  $N_2$  vibrational and electronic excitation. We have numerically simulated the ionospheric feedback instability in strong SAID flows with depleted density profiles. The simulations show that the IFI generates strong, small-scale field-aligned currents and enhanced parallel electric fields,  $E_{\parallel}$ , below the  $F_2$  peak. The magnitude of  $E_{\parallel}$  nonlinearly increases with the SAID flow velocity and the density depletion. The generated field controls the electron distribution function (EDF), which determines the power going to the excitation and ionization of neutral gas (the energy balance). Because at altitudes below  $\sim 250$  km the EDF strongly deviates from a Maxwellian distribution, we employed a rigorous numerical solution of the Boltzmann kinetic equation in the whole range of the  $E_{\parallel}$  magnitudes. The resulting energy balance at altitudes of 130–140 km corresponds to the suprathermal electron population and excited neutral species in good quantitative agreement with that required for Picket Fence. The theory predictions are also consistent with the STEVE enhanced continuum and redline emissions above 200 km. Moreover, inside SAID channels with strongly depleted density, the IFI-generated fields create many ionizing electrons at altitudes of  $\sim 150$ –200 km. Because of additional ionization, the initial density profile changes with time. It is anticipated that the IFI development in the evolving density profile will be saturated when the generated fields in the whole altitude range reduce below the ionization threshold. In other words, subauroral arcs might have the transient phase with typical aurora-like emissions that fade out afterward.

#### Data Availability Statement

The paper does not produce any new experimental data and numerical codes.

#### Acknowledgments

E.V.M. and A.V.S. acknowledge support by the Air Force Office of Scientific Research LRIR 22RVCOR011 and the NSF award AGS 1803702, respectively. Approved for public release; distribution is unlimited. Public Affairs release approval #AFRL-2022-2640. The views expressed are those of the authors and do not reflect the official guidance or position of the United States Government, the Department of Defense or of the United States Air Force. The appearance of external hyperlinks does not constitute endorsement by the United States Department of Defense (DoD) of the linked websites, or the information, products, or services contained therein. The DoD does not exercise any editorial, security, or other control over the information you may find at these locations.

#### References

- Akbari, H., Pfaff, R., Clemmons, J., Freudenreich, H., Rowland, D., & Streltsov, A. (2022). Resonant Alfvén waves in the lower auroral ionosphere: Evidence for the nonlinear evolution of the ionospheric feedback instability. *Journal of Geophysical Research: Space Physics*, *127*(2), e2021JA029854. <https://doi.org/10.1029/2021JA029854>
- Allan, W. (1983). Quarter-wave ULF pulsations. *Planetary and Space Science*, *31*(3), 323–330. [https://doi.org/10.1016/0032-0633\(83\)90083-1](https://doi.org/10.1016/0032-0633(83)90083-1)
- Allan, W., & Knox, F. (1979). The effect of finite ionosphere conductivities on axisymmetric toroidal Alfvén wave resonances. *Planetary and Space Science*, *27*(7), 939–950. [https://doi.org/10.1016/0032-0633\(79\)90024-2](https://doi.org/10.1016/0032-0633(79)90024-2)
- Archer, W., Gallardo-Lacourt, B., Perry, G., St.-Maurice, J. P., Buchert, S., & Donovan, E. (2019). STEVE: The optical signature of intense subauroral ion drifts. *Geophysical Research Letters*, *46*(12), 6279–6286. <https://doi.org/10.1029/2019GL082687>
- Archer, W., St.-Maurice, J. P., Gallardo-Lacourt, B., Perry, G., Cully, C., Donovan, E., et al. (2019). The vertical distribution of the optical emissions of a STEVE and Picket Fence event. *Geophysical Research Letters*, *46*(19), 10719–10725. <https://doi.org/10.1029/2019GL084473>
- Banks, P., Chappell, C., & Nagy, A. (1974). A new model for the interaction of auroral electrons with the atmosphere: Spectral degradation, backscatter, optical emission, and ionization. *Journal of Geophysical Research*, *79*(10), 1459–1470. <https://doi.org/10.1029/ja079i010p01459>
- Budnik, F., Stellmacher, M., Glassmeier, K.-H., & Buchert, S. C. (1998). Ionospheric conductance distribution and MHD wave structure: Observation and model. In *Annales de Geophysique* (Vol. 16(2), pp. 140–147). Copernicus GmbH. <https://doi.org/10.1007/s00585-998-0140-8>
- Capitelli, M., Ferreira, C., Gordiets, B., & Osipov, A. (2000). *Plasma kinetics in atmospheric gases*. Springer.
- Chu, X., Malaspina, D., Gallardo-Lacourt, B., Liang, J., Andersson, L., Ma, Q., et al. (2019). Identifying STEVE's magnetospheric driver using conjugate observations in the magnetosphere and on the ground. *Geophysical Research Letters*, *46*(22), 12665–12674. <https://doi.org/10.1029/2019GL082789>
- Dyatko, N., Kochetov, I., Mishin, E., & Telegin, V. (1989). The kinetics of electrons in a weakly ionized ionospheric plasma. *Geomagnetism and Aeronomy*, *29*, 241–245.
- Galeev, A., & Sagdeev, R. (1984). Current instabilities and anomalous resistivity of plasmas. In A. Galeev & R. Sudan (Eds.), *Basic plasma physics* (pp. 271–335). Elsevier. V. 2 (suppl.).
- Gallardo-Lacourt, B., Liang, J., Nishimura, Y., & Donovan, E. (2018). On the origin of STEVE: Particle precipitation or ionospheric skyglow? *Geophysical Research Letters*, *45*(16), 7968–7973. <https://doi.org/10.1029/2018gl078509>
- Gallardo-Lacourt, B., Nishimura, Y., Donovan, E., Gillies, D., Perry, G., Archer, W., et al. (2018). A statistical analysis of STEVE. *Journal of Geophysical Research: Space Physics*, *123*(11), 9893–9905. <https://doi.org/10.1029/2018JA025368>
- Gillies, D., Donovan, E., Hampton, D., Liang, J., Connors, M., Nishimura, Y., et al. (2019). First observations from the TReX Spectrograph: The optical spectrum of STEVE and the Picket Fence phenomena. *Geophysical Research Letters*, *46*(13), 7207–7213. <https://doi.org/10.1029/2019GL083272>
- Gurevich, A. (1978). *Nonlinear phenomena in the ionosphere* (p. 370). Springer.

- Henderson, M. (2021). Generation of subauroral longitudinally extended emissions following intensifications of the poleward boundary of the substorm bulge and streamer production. *Journal of Geophysical Research: Space Physics*, 126(3), e2020JA028556. <https://doi.org/10.1029/2020JA028556>
- Hunnekuhl, M., & MacDonald, E. (2020). Early ground-based work by auroral pioneer Carl Stormer on the high-altitude detached subauroral arcs now known as "STEVE". *Space Weather*, 18(3), e2019SW002384. <https://doi.org/10.1029/2019SW002384>
- Itikawa, Y. (2006). Cross sections for electron collisions with nitrogen molecules. *Journal of Physical and Chemical Reference Data*, 35(1), 31–53. <https://doi.org/10.1063/1.1937426>
- Jia, N., & Streltsov, A. (2014). Ionospheric feedback instability and active discrete auroral forms. *Journal of Geophysical Research: Space Physics*, 119(3), 2243–2254. <https://doi.org/10.1002/2013ja019217>
- Khazanov, G., Sibeck, D., & Zesta, E. (2017). Major pathways to electron distribution function formation in regions of diffuse aurora. *Journal of Geophysical Research: Space Physics*, 122(4), 4251–4265. <https://doi.org/10.1002/2017JA023956>
- Konovalov, V., & Son, E. (2015). Degradation spectra of electrons in the ionosphere. In *Journal of physics: Conference series* (Vol. 653, p. 012120). IOP Publishing. <https://doi.org/10.1088/1742-6596/653/1/012120>
- Liang, J., Donovan, E., Connors, M., Gillies, D., St-Maurice, J.-P., Jackel, B., et al. (2019). Optical spectra and emission altitudes of double-layer STEVE: A case study. *Geophysical Research Letters*, 46(23), 13630–13639. <https://doi.org/10.1029/2019GL085639>
- MacDonald, E., Donovan, E., Nishimura, Y., Case, N., Gillies, D. M., Gallardo-Lacourt, B., et al. (2018). New science in plain sight: Citizen scientists lead to the discovery of optical structure in the upper atmosphere. *Science Advances*, 4(3), eaaq0030. <https://doi.org/10.1126/sciadv.aaq0030>
- Majeed, T., & Strickland, D. (1997). New survey of electron impact cross sections for photoelectron and auroral electron energy loss calculations. *Journal of Physical and Chemical Reference Data*, 26(2), 335–349. <https://doi.org/10.1063/1.556008>
- Mende, S. B., Harding, B. J., & Turner, C. (2019). Subauroral green STEVE arcs: Evidence for low-energy excitation. *Geophysical Research Letters*, 46(14), 14256–14262. <https://doi.org/10.1029/2019GL086145>
- Mende, S. B., & Turner, C. (2019). Color ratios of subauroral (STEVE) arcs. *Journal of Geophysical Research: Space Physics*, 124(7), 5945–5955. <https://doi.org/10.1029/2019JA026851>
- Mikhailovskii, A. (1974). *Theory of plasma instabilities: Instabilities of a homogeneous plasma* (Vol. 1). Consultants Bureau.
- Milikh, G., & Dimant, Y. (2003). Model of anomalous electron heating in the E region: 2. Detailed numerical modeling. *Journal of Geophysical Research*, 108(A9), 1351. <https://doi.org/10.1029/2002JA009527>
- Mishin, E. (2013). Interaction of substorm injections with the subauroral geospace: 1. Multispacecraft observations of SAID. *Journal of Geophysical Research: Space Physics*, 118(9), 5782–5796. <https://doi.org/10.1002/jgra.50548>
- Mishin, E., Burke, W., & Pedersen, T. (2004). On the onset of HF-induced airglow at HAARP. *Journal of Geophysical Research*, 109(A2), A02305. <https://doi.org/10.1029/2003JA010205>
- Mishin, E., Carlson, H., & Hagfors, T. (2000). On the electron distribution function in the F region and airglow enhancements during HF modification experiments. *Geophysical Research Letters*, 27(18), 2857–2860. <https://doi.org/10.1029/2000gl000075>
- Mishin, E., & Streltsov, A. (2019). STEVE and the picket fence: Evidence of feedback-unstable magnetosphere-ionosphere interaction. *Geophysical Research Letters*, 46(14), 14247–14255. <https://doi.org/10.1029/2019GL085446>
- Mishin, E., & Streltsov, A. (2021). *Nonlinear wave and plasma structures in the auroral and subauroral geospace* (p. 621). Elsevier.
- Nishimura, Y., Gallardo-Lacourt, B., Zou, Y., Mishin, E., Knudsen, D. J., Donovan, E. F., & Raybell, R. (2019). Magnetospheric signatures of STEVE: Implications for the magnetospheric energy source and interhemispheric conjugacy. *Geophysical Research Letters*, 46(11), 5637–5644. <https://doi.org/10.1029/2019GL082460>
- Obana, Y., Menk, F. W., Sciffer, M. D., & Waters, C. L. (2008). Quarter-wave modes of standing Alfvén waves detected by cross-phase analysis. *Journal of Geophysical Research*, 113(A8), A08203. <https://doi.org/10.1029/2007JA012917>
- Obana, Y., Waters, C. L., Sciffer, M. D., Menk, F. W., Lysak, R. L., Shiokawa, K., et al. (2015). Resonance structure and mode transition of quarter-wave ULF pulsations around the dawn terminator. *Journal of Geophysical Research: Space Physics*, 120(6), 4194–4212. <https://doi.org/10.1002/2015JA021096>
- Picone, J., Hedin, A., Drob, D., & Aikin, A. (2002). NRLMSISE-00 empirical model of the atmosphere: Statistical comparisons and scientific issues. *Journal of Geophysical Research*, 107(A12), 1468. <https://doi.org/10.1029/2002ja009430>
- Piper, L. (1992). Energy transfer studies on N<sub>2</sub>(X, V) and N<sub>2</sub>(B). *The Journal of Chemical Physics*, 97(1), 270–275. <https://doi.org/10.1063/1.463625>
- Streltsov, A., Jia, N., Pedersen, T., Frey, H., & Donovan, E. (2012). ULF waves and discrete aurora. *Journal of Geophysical Research*, 117(A9), A09227. <https://doi.org/10.1029/2012JA017644>
- Streltsov, A., & Mishin, E. (2018). Ultralow frequency electrodynamic of magnetosphere-ionosphere interactions near the plasma pause during substorms. *Journal of Geophysical Research: Space Physics*, 123(9), 7441–7451. <https://doi.org/10.1029/2018JA025899>
- Streltsov, A. V. (2018). On the asymmetry between upward and downward field-aligned currents interacting with the ionosphere. *Journal of Geophysical Research: Space Physics*, 123(11), 9275–9285. <https://doi.org/10.1029/2018JA025826>
- Titheridge, J. (2003). Ionization below the night F2 layer—A global model. *Journal of Atmospheric and Solar-Terrestrial Physics*, 65(9), 1035–1052. [https://doi.org/10.1016/S1364-6826\(03\)00136-6](https://doi.org/10.1016/S1364-6826(03)00136-6)
- Trakhtengertz, V., & Feldstein, A. (1991). Turbulent Alfvén boundary layer in the polar ionosphere. 1. Excitation conditions and energetics. *Journal of Geophysical Research*, 96(A11), 19363–19374. <https://doi.org/10.1029/91ja00376>
- Voronkov, I., & Mishin, E. (1993). Quasilinear regime of Langmuir turbulence in the auroral E region of the ionosphere. *Geomagnetism and Aeronomy*, 33, 350–355.